43rd AIAA Fluid Dynamics Conference
June 24-27, 2013, San Diego, CA

AIAA 2013-2734

Analysis of the Large Eddy Simulation of a Shock Wave and Turbulent Boundary Layer Interaction

Justine Li,* Stephan Priebe,† Nathan Grube,‡
and M. Pino Martín§

The large eddy simulation (LES) of a compression ramp shock wave and turbulent boundary layer interaction (STBLI) is presented. The ramp angle is $24°$ and the incoming boundary layer flow conditions are Mach 2.9 and Re$_\theta$ 2900. The LES data cover approximately 1300 L_{sep}/U_∞ to statistically resolve the aperiodic cycle of the low-frequency unsteadiness that is characteristic of these types of flows. The dynamics of the flow downstream of the shock are characterized using this new numerical data set.

Nomenclature

f	frequency
f_s	shock frequency
t	time
p	pressure
ρ	density
u, v, w	streamwise, spanwise, and wall-normal velocity
U_∞	freestream velocity
ν	kinematic viscosity
M	Mach number
δ	99% boundary layer thickness
θ	compressible momentum thickness
Re_θ	Reynolds number based on momentum thickness, θ, and freestream values U_∞ and ν_∞
C_f	skin-friction coefficient
L_{sep}	time- and spanwise-averaged separation length
S_L	shock Strouhal number
x, y, z	physical coordinates in streamwise, spanwise, and wall-normal directions

Superscript

$*$	coordinates referenced to compression corner location

Subscript

w	wall quantity
∞	freestream quantity

I. Introduction

A common and important flow feature in compressible flow applications is the interaction of a shock wave with a turbulent boundary layer. In cases where the mean flow is separated, a low-frequency unsteadiness (that is one to two orders of magnitude lower in frequency than the characteristic frequency of the incoming

*Graduate Student, Department of Aerospace Engineering, University of Maryland, College Park.
†Research Associate, Department of Aerospace Engineering, University of Maryland, College Park.
‡Faculty Research Assistant, Department of Aerospace Engineering, University of Maryland, College Park.
§AIAA Associate Fellow. Associate Professor, Department of Aerospace Engineering, University of Maryland, College Park.

turbulent boundary layer) is characteristic of these flows. The unsteadiness and the associated large pressure and heat transfer loads have detrimental effects on supersonic and hypersonic engineering systems.

In Dussauge et al.,[1] the authors found that in a range of configurations including the compression ramp at a range of Mach and Reynolds numbers, the dimensionless shock frequency number, $S_L = f_s L_{sep}/U_e$, where f_s is the characteristic shock frequency, L_{sep} is the separation length, and U_e is the external velocity, lies in the range of $S_L = 0.02 - 0.05$ regardless of geometric configuration.

The cause of the low-frequency unsteadiness is still under debate. It has been proposed that the shock motion is due to the upstream boundary layer, see e.g. Ganapathisubramani, Clemens and Dolling,[2] or, alternatively, that it is due to the downstream separated flow, see e.g. Dupont et al.,[3] Dussauge et al.,[1] and Piponniau et al.[4] The ability of LES to capture the important physical aspects of STBLI flows has been demonstrated (e.g. Garnier, Sagaut and Deville;[5] Loginov, Adams and Zheltovodov;[6] Touber and Sandham;[7] Morgan, Kawai and Lele;[8] Hadjadj;[9] and Grilli, Hickel, and Adams[10]). Developments in large eddy simulations (LESs) show the ability to capture the characteristic low-frequency unsteadiness of the flow, enabling investigation into its origins. Touber and Sandham[7] performed the LES of a reflected STBLI at Mach 2.3 and Re_θ 5900, matching experimental flow conditions.[1] The low-frequency unsteadiness is present in their simulations at the same frequency as in experiments. A stability analysis is also performed, and this shows the presence of a global instability mode which could be connected to the observed low-frequency unsteadiness. Grilli et al.[10] performed the LES of a 25°compression-expansion ramp flow at Mach 2.88. The authors were able to capture the low-frequency unsteady motion in the main shock, showing similar results to the direct numerical simulation (DNS) of Wu and Martín, 2008.[11]

The DNS data presented in Priebe and Martín, 2012[12] for the Mach 2.9, 24° compression ramp flow at $Re_\theta = 2900$ were collected at sufficiently high frequency to characterize the low-frequency unsteadiness. The shock motion characteristic of these flows was found to be related to the evolution of the separation bubble. This DNS data were gathered at high-frequency to acquire the time-resolved evolution of the spanwise-averaged flow field. The separation bubble phases can be seen in the low-pass filtered DNS flow fields in Priebe and Martín, 2012.[12] In this analysis, the authors describe the relationship between shock motion, the separation bubble size, and the structure of the shear layer. Due to the computational cost of the DNS in generating the high-frequency flow field data, only a few detailed simulations were presented. Since DNS is computationally expensive compared to LES, the ability to converge the conditional statistics on the aperiodic motion has remained elusive.

The long duration LES data of the Mach 2.9, Re_θ 2900 flow for the 24° compression ramp configuration and validation against existing DNS data for the same conditions are presented. The data presented here are generated using the same numerical methods for the same computational setup as our previous LES, but does not include the data presented in Li, Grube, Priebe, and Martín.[13] In Section II, the numerical methods and computational setup used in this simulation are briefly reviewed. Results of the LES of the compression ramp flow are presented in Section III; Section A shows the time- and spanwise-averaged streamwise distribution and flowfield of this simulation, and Sections B and C present several high-frequency time signals and their spectra. Finally, Section D presents the analysis of a detailed simulation suggesting that the LES captures the flow field evolution associated with the separation bubble phases. Analysis of the long-duration LES data and a detailed simulation demonstrates the ability of this LES code to capture low-frequency shock motion characteristic of STBLI and separation bubble phases in the compression ramp configuration.

II. Numerical Methods and Computational Setup

The numerical scheme and general computational setup used in the LES are the same as those used in the previous simulations by Wu and Martín.[14] For the discretization of the inviscid fluxes, we use a 4th-order accurate weighted essentially non-oscillatory scheme (WENO), which is both linearly and non-linearly optimized.[14–16] For the spatial discretization of the viscous fluxes, 4th-order accurate central differencing is used, and time-integration is performed with a 3rd-order accurate, low-storage Runge-Kutta algorithm. The LES solves the Favre-filtered Navier-Stokes equations on a coarse grid; the subgrid scale stresses and heat fluxes are modeled using the one-coefficient dynamic mixed model and the subgrid scale turbulent kinetic energy diffusion term is modeled by Knight et al., 1998.[17] Further information on the subgrid scale models used in this simulation is provided in Martín, Piomelli and Candler.[18]

The code in DNS mode was validated by Wu and Martín[14] (in terms of the separation length, mean wall pressure distribution and velocity profiles through the interaction) against the experiments of Bookey, Wyckham and Smits[19] at matching flow conditions. In addition, the fluctuating wall pressure in Wu and Martín's DNS was validated by Ringuette, Wu and Martín[20] against the experiments of Ringuette and Smits,[21] and Ringuette et al.[22] Preliminary data generated using this code in LES mode demonstrate its ability to capture salient flow features for the compression ramp configuration. Further details regarding the numerical methods and computational setup for this LES can be found in Li, Grube, Priebe, and Martín.[13]

III. Results

A. Time- and Spanwise-averaged Results

Statistics of the flow are gathered over 3500 δ/U_∞, approximately 10 times the simulation length of the previous LES and almost four times the simulation length of the DNS in Priebe and Martín.[12] Full flowfield data are gathered at a frequency of approximately 1 U_∞/δ and high-frequency data planes are gathered at about 400 U_∞/δ. These spanwise-wall normal planes sample the different regions of the flow at high frequency, such as the incoming boundary layer, the separated region, and downstream of the interaction region. The planes are then spanwise averaged to compute high-frequency time signals.

The time- and spanwise-averaged separation point and reattachment point are $x^*_{sep}/\delta = -2.16$ and $x^*_{rea}/\delta = 0.59$ respectively. The average separation length is $L_{sep} = 2.75\delta$, a decrease of 8% from the DNS.[12] In Figure 1, it can be seen that the LES has a similar separated region at the corner and that the wall-pressure in the incoming turbulent boundary layer and downstream of the interaction region is well-predicted.

B. High-Frequency Time Signals

High-frequency, spanwise-averaged signals were collected at a frequency of approximately 400 U_∞/δ from the LES to analyze the unsteadiness of the flow. The separation and reattachment points' signals are used to gauge the size of the separated region at the corner. The instantaneous separation point is computed as the most upstream point where the $C_f = 0$ and $\frac{\partial C_f}{\partial x} < 0$. Similarly, the instantaneous reattachment point is computed as the most downstream point where the $C_f = 0$ and $\frac{\partial C_f}{\partial x} > 0$. Both the separation and reattachment signals and their respective low-pass filtered signals (cutoff $S_L = 0.22$) are shown in Figure 2. In the separation point signal, the low-frequency aperiodic shock motion can be seen with a period corresponding to a frequency on the order of $O(0.1U_\infty/L_{sep})$.

A series of wall pressure signals were gathered at streamwise points of interest: near the inlet (x^*/δ = -5.05), upstream of the time-averaged separation point (x^*/δ = -2.36), downstream of the time-averaged separation point (x^*/δ = -1.86), and near the time-averaged reattachment point ($x^*/\delta = 0.60$). These signals will be used to analyze the evolution of the frequency content of the flow in the streamwise direction. In order to quantify the frequency content of the signals, power spectra are calculated for each of the signals.

C. Spectra of High-Frequency Time signals

The spectra are estimated using Welch's method in which the signal is divided into overlapping segments. The data on each segment is weighted using a Hamming window. In this case, the segment length is approximately 236 δ/U_∞ for a total of 29 segments with 50% overlap. Further details on the method used here can be seen in Priebe and Martín, 2012.[12]

The separation point spectrum in Figure 3 shows two peaks at $fL_{sep}/U_\infty = 0.07$ and 0.3. The lower frequency is of the same magnitude as the low-frequency peak seen in the DNS of Priebe and Martín, 2012.[12] The higher frequency peak at $fL_{sep}/U_\infty = 0.3$ is due to the rescaling method to generate the boundary conditions at the inlet as described in Xu and Martín, 2004.[23] The broadband peak of the reattachment signal in Figure 4 is centered around $fL_{sep}/U_\infty = 0.5$, consistent with the DNS results.

The wall pressure spectra demonstrate the effect of the low-frequency unsteadiness at various streamwise locations. At the inlet, the wall pressure spectrum, shown in Figure 5a, shows that the characteristic frequency of the incoming boundary layer is approximately 1 U_∞/δ with negligible frequency content under $fL_{sep}/U_\infty = 0.1$, which are the frequencies associated with the low-frequency shock motion. Just upstream of the time- and spanwise-averaged separation point, the wall pressure signal spectrum (Figure 5b) peaks at approximately $fL_{sep}/U_\infty = 0.06$. Similarly, the wall pressure spectrum at a slightly downstream location of the time- and spanwise-averaged separation point (Figure 5c) shows the frequency content at this location is centered at approximately $fL_{sep}/U_\infty = 0.02$. The peaks of these spectra of wall pressure signals near the separation point are consistent with the findings of Priebe and Martín, 2012,[12] and Dussauge et al.[1] In Figure 5d, the wall pressure signal spectrum at the time- and spanwise-averaged reattachment location shows that there is less low-frequency content compared to higher frequency content near reattachment.

D. Low-pass filtered, spanwise-averaged flow fields

Priebe and Martín, 2012[12] have observed changes in the flow field dependent on the phase of the separation bubble. Figure 6 are schematics of the flow features during bubble growth (a) and bubble collapse (b). During separation bubble growth, the shock wave is moving upstream, the separated shear layer is large and extends above the separation bubble, and the skin friction coefficient, C_f between the instantaneous separation and reattachment points remains below $C_f = 0$. Alternatively, when the separation bubble collapses, the shockwave is moving downstream towards the corner, a second branch of large spanwise vorticity appears along the wall leading up to the corner in addition to the separated shear layer above the separation bubble, and the C_f between the separation and reattachment points is higher than the C_f during separation bubble growth. Previous analysis of time-resolved DNS data[12] show the evolution of the separation bubble and associated flow field changes.

In order to perform the time-resolved flow field analysis, a detailed simulation is completed for $t_{span}U_\infty/\delta$ $= 357.1$ ($tU_\infty/\delta = 1510.9$ to 1868.0). Time-resolved flow fields were captured at $f\delta/U_\infty = 10.2$ throughout this simulation. The flow field at each instant is low-pass filtered using a finite impulse response (FIR) filter with a cutoff Strouhal number of 0.22. The filter spans 30 $\delta/U\infty$ and is consistent with the one used in the analysis of the detailed DNS simulation.[12]

The separation and reattachment point signals over the duration of the detailed simulation is shown in Figure 7. The vertical lines show the instants at which the shock is moving downstream (a, d) corresponding to separation bubble collapse as well as the instants at which the shock is moving upstream (b, c) which correspond to separation bubble growth. In Figure 8a, the spanwise-averaged low-pass filtered flow field during the first bubble collapse in the detailed simulation is shown. Subsequently, in Figure 8b, the separation bubble is growing and there is one large region of high spanwise vorticity. A slight structural change can be seen in the separated shear layer, visualized by the regions of high spanwise vorticity. A change in the separation bubble can also be seen in the streamline traces on these figures. In Figure 8a during bubble collapse, there are two small recirculating regions; in contrast, Figure 8b has a single, elongated recirculating region at the corner. Figure 9 compares the instantaneous, low-pass filtered skin friction coefficient, C_f, distribution between instants (a) and (b). For both instances, it can be seen that the $C_f \leq 0$ in the separated region with a local maximum located in the middle. In the separated region, the C_f at the instant of the downstream moving shock (a) is marginally greater than the C_f at the instant of the upstream moving shock (b). The LES shows that the C_f is generally larger in the separated region during the bubble's collapse when compared to the C_f during the bubble's growth. This is consistent with the previous DNS results of Priebe and Martin,[12] but in the present LES the difference in the C_f between bubble phases has a much lower-amplitude difference than in the DNS. It should be noted that these distributions contain noise, such that no conclusions can be drawn from the LES data. The difference in the shape of the instantaneous, low-pass filtered C_f distributions as compared to the DNS[12] can be expected as the time- and spanwise-averaged C_f distributions for the LES and DNS are different as well.

Likewise, for the separation bubble growth and collapse as captured in instances (c) and (d), similar structures can be seen. In Figures 10c and d, there is a slight change in the spanwise vorticity field. Figure 10c shows a similar single, elongated recirculating region during bubble expansion as in Figure 8b. During this bubble collapse, as visualized in Figure 10d, the recirculating region at the corner appears to have disappeared entirely. The skin friction coefficients for the two instances are compared in Figure 11. Much like the previous instantaneous, low-pass filtered C_f distributions, the C_f in the separated region during downstream shock motion and bubble collapse remains higher than the distribution during upstream shock motion despite the noise in the distributions. It is difficult to conclude whether or not the differences in the flow field at different phases of separation bubble evolution are significant based on two samples; however, these two samples of separation bubble growth and collapse suggest that the LES is able to capture a similar physical mechanism as seen in the DNS.[12]

IV. Conclusion

Analysis of the long duration LES data of the Mach 2.9 Re_θ 2900 flow for the 24° compression ramp configuration in comparison to the DNS data[12] of the same configuration demonstrates the LES code's capability to capture the low-frequency unsteadiness characteristic of these flows. Analysis of LES time signals and their respective spectra suggests that we are able to simulate the low-frequency shock motion and the flowfield's evolution through time using this LES code. Performing analysis as previously done on the DNS[12] data, the low-pass filtered, spanwise-averaged flow fields suggest that the flow structures change depending on the phase of separation bubble evolution.

Acknowledgments

This work is supported by the Air Force Office of Scientific Research under grants AF/9550-10-1-0164 and AF/9550-09-1-0464, and by the Department of Defense through the National Defense Science and Engineering Graduate Fellowship Program.

References

[1] Dussauge, J. P., Dupont, P., and Debiève, J. F., "Unsteadiness in Shock Wave Boundary Layer Interactions with Separation," *Aerospace Science and Technology*, Vol. 10, No. 2, 2006.

[2] Ganapathisubramani, B., Clemens, N. T., and Dolling, D. S., "Effects of upstream boundary layer on the unsteadiness of shock-induced separation," *Journal of Fluid Mechanics*, Vol. 585, 2007, pp. 369–394.

[3] Dupont, P., Haddad, C., and Debiève, J. F., "Space and time organization in a shock-induced separated boundary layer," *Journal of Fluid Mechanics*, Vol. 559, 2006, pp. 255–277.

[4] Piponniau, S., Dussauge, J., Debiève, J., and Dupont, P., "A simple model for low-frequency unsteadiness in shock-induced separation," *Journal of Fluid Mechanics*, Vol. 629, 2009, pp. 87–108.

[5] Garnier, E., Sagaut, P., and Deville, M., "Large Eddy Simulation of Shock/Boundary-Layer Interaction," *AIAA Journal*, Vol. 40, No. 10, 2002, pp. 1935–1944.

[6] Loginov, M. S., Adams, N. A., and Zheltovodov, A. A., "Large-eddy simulation of shock-wave/turbulent-boundary-layer interaction," *Journal of Fluid Mechanics*, Vol. 565, 2006, pp. 135–169.

[7] Touber, E. and Sandham, N., "Large-eddy simulation of low-frequency unsteadiness in a turbulent shock-induced separation bubble," *Theoretical and Computational Fluid Dynamics*, Vol. 23, 2009, pp. 79–107.

[8] Morgan, B., Kawai, S., and Lele, S. K., "Large-Eddy Simulation of an Oblique Shock Impinging on a Turbulent Boundary Layer," *AIAA Paper No. 2010-4467*, June 2010.

[9] Hadjadj, A., "Large-Eddy Simulation of Shock/Boundary-Layer Interaction," *AIAA Journal*, Vol. 50, No. 12, 2012, pp. 2919–2927.

[10] Grilli, M., Hickel, S., and Adams, N., "Large-eddy simulation of a supersonic turbulent boundary layer over a compression-expansion ramp," *International Journal of Heat and Fluid Flow*, 2013.

[11] Wu, M. and Martín, M. P., "Analysis of Shock Motion in Shockwave and Turbulent Boundary Layer Interaction using Direct Numerical Simulation Data," *Journal of Fluid Mechanics*, Vol. 594, 2008, pp. 71–83.

[12] Priebe, S. and Martín, M. P., "Low-frequency unsteadiness in shock wave-turbulent boundary layer interaction," *Journal of Fluid Mechanics*, Vol. 699, 2012.

[13] Li, J., Grube, N., Priebe, S., and Martín, M., "LES Study of Shock Wave and Turbulent Boundary Layer Interaction," *AIAA Paper No. 2013-0984*, January 2013.

[14] Wu, M. and Martín, M. P., "Direct Numerical Simulation of Supersonic Turbulent Boundary Layer over a Compression Ramp," *AIAA Journal*, Vol. 45, No. 4, 2007, pp. 879–889.

[15] Martín, M. P., Taylor, E. M., Wu, M., and Weirs, V. G., "A Bandwidth-Optimized WENO Scheme for the Direct Numerical Simulation of Compressible Turbulence," *Journal of Computational Physics*, Vol. 220, 2006, pp. 270–289.

[16] Taylor, E. M., Wu, M., and Martín, M. P., "Optimization of Nonlinear Error Sources for Weighted Essentially Non-oscillatory Methods in Direct Numerical Simulations of Compressible Turbulence," *Journal of Computational Physics*, Vol. 223, 2007, pp. 384–397.

[17] Knight, D., Zhou, G., Okong'o, N., and Shukla, V., "Compressible Large Eddy Simulation Using Unstructured Grids," *AIAA Paper No. 98-0535*, 1998.

[18] Martín, M. P., Piomelli, U., and Candler, G. V., "Subgrid-scale Models for Compressible LES," *Theoretical and Computational Fluid Dynamics*, Vol. 13, 2000.

[19] Bookey, P. B., Wyckham, C., and Smits, A. J., "Experimental Investigations of Mach 3 Shock-Wave Turbulent Boundary Layer Interactions," *AIAA Paper No. 2005-4899*, June 2005.

[20] Ringuette, M. J., Wu, M., and Martín, M. P., "Low Reynolds Number Effects in a Mach 3 Shock Turbulent Boundary Layer Interaction," *AIAA Journal*, Vol. 46, No. 7, 2008.

[21] Ringuette, M. J. and Smits, A. J., "Wall-Pressure Measurements in a Mach 3 Shock-Wave and Turbulent Boundary Layer Interaction at a DNS-Accessible Reynolds Number," *AIAA Paper No. 2007-4113*, June 2007.

[22] Ringuette, M. J., Bookey, P., Wyckham, C., and Smits, A. J., "Experimental Study of a Mach 3 Compression Ramp Interaction at $\mathrm{Re}_\theta = 2400$," *AIAA Journal*, Vol. 47, 2009, pp. 373–385.

[23]Xu, S. and Martín, M. P., "Inflow Boundary Conditions for Compressible Turbulent Boundary Layers," *AIAA Paper No. 2003-3963*, 2003.

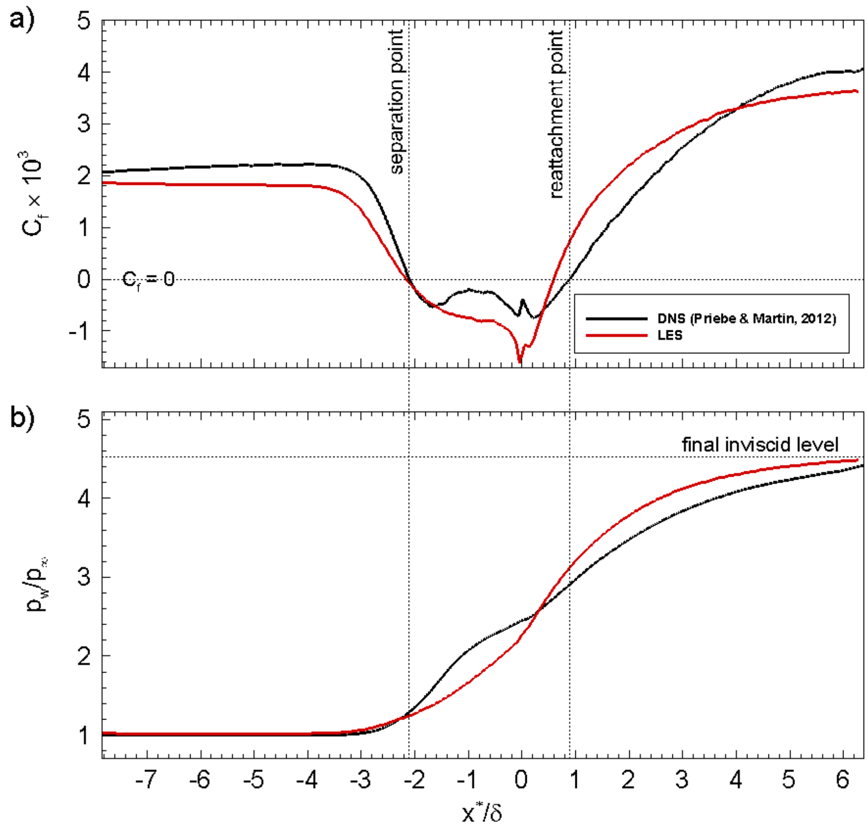

Figure 1. Time- and spanwise-averaged distribution of: (*a*) skin friction coefficient C_f; and (*b*) wall-pressure

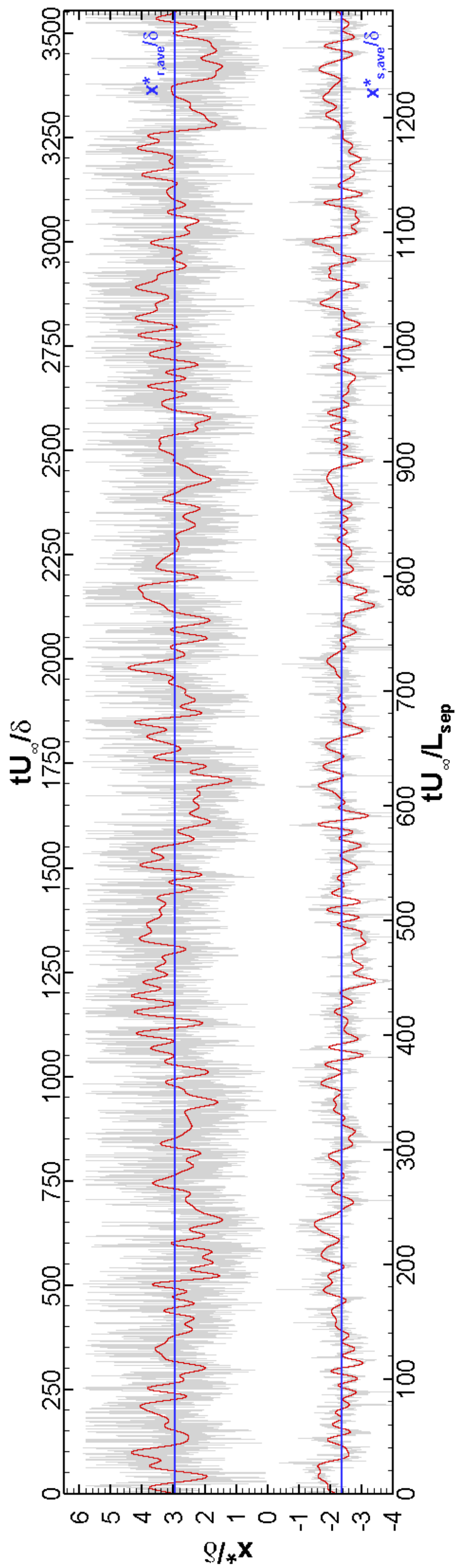

Figure 2. Separation and reattachment location signals; raw signal in gray (the lowpass filtered signal, cutoff $S_L = 0.22$, in red)

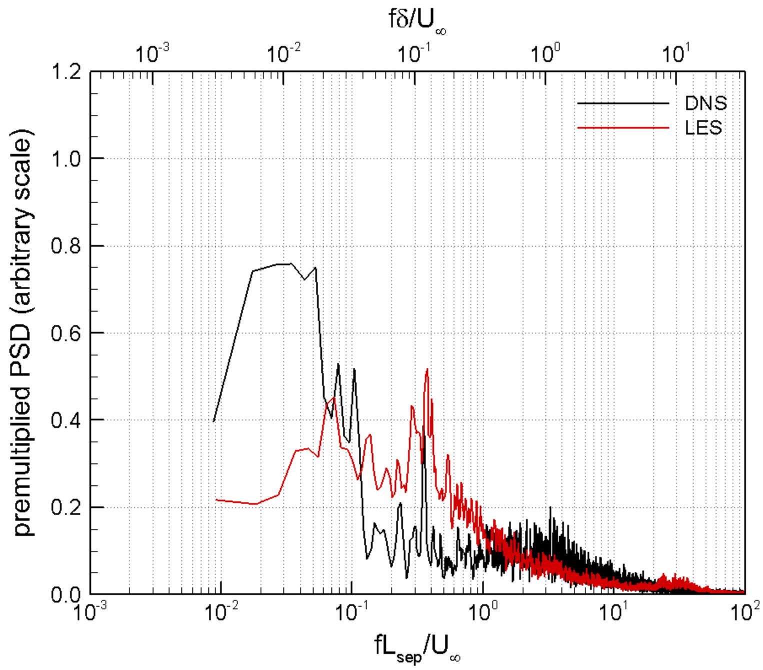

Figure 3. Separation location signal spectrum (red) with DNS[12] spectrum (black)

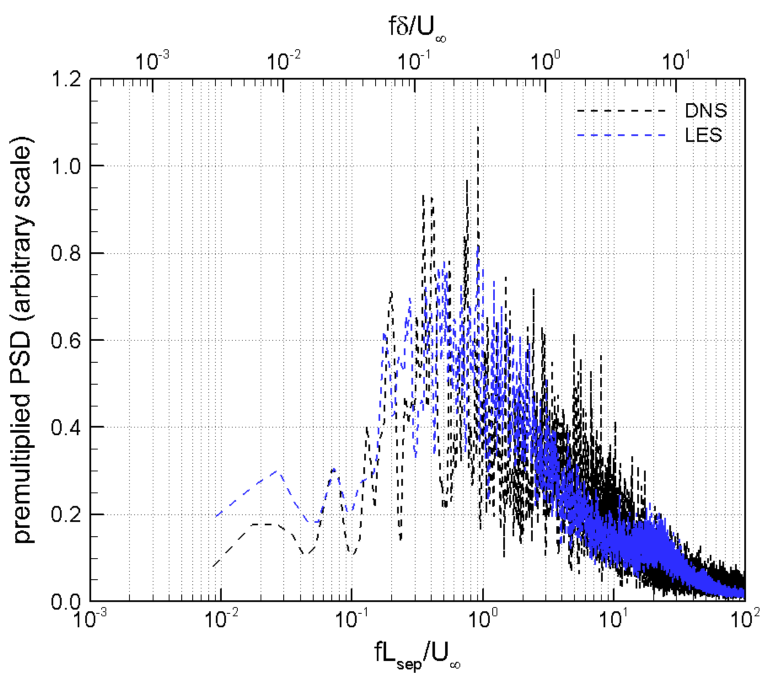

Figure 4. Reattachment location signal spectrum (blue) with DNS[12] spectrum (black)

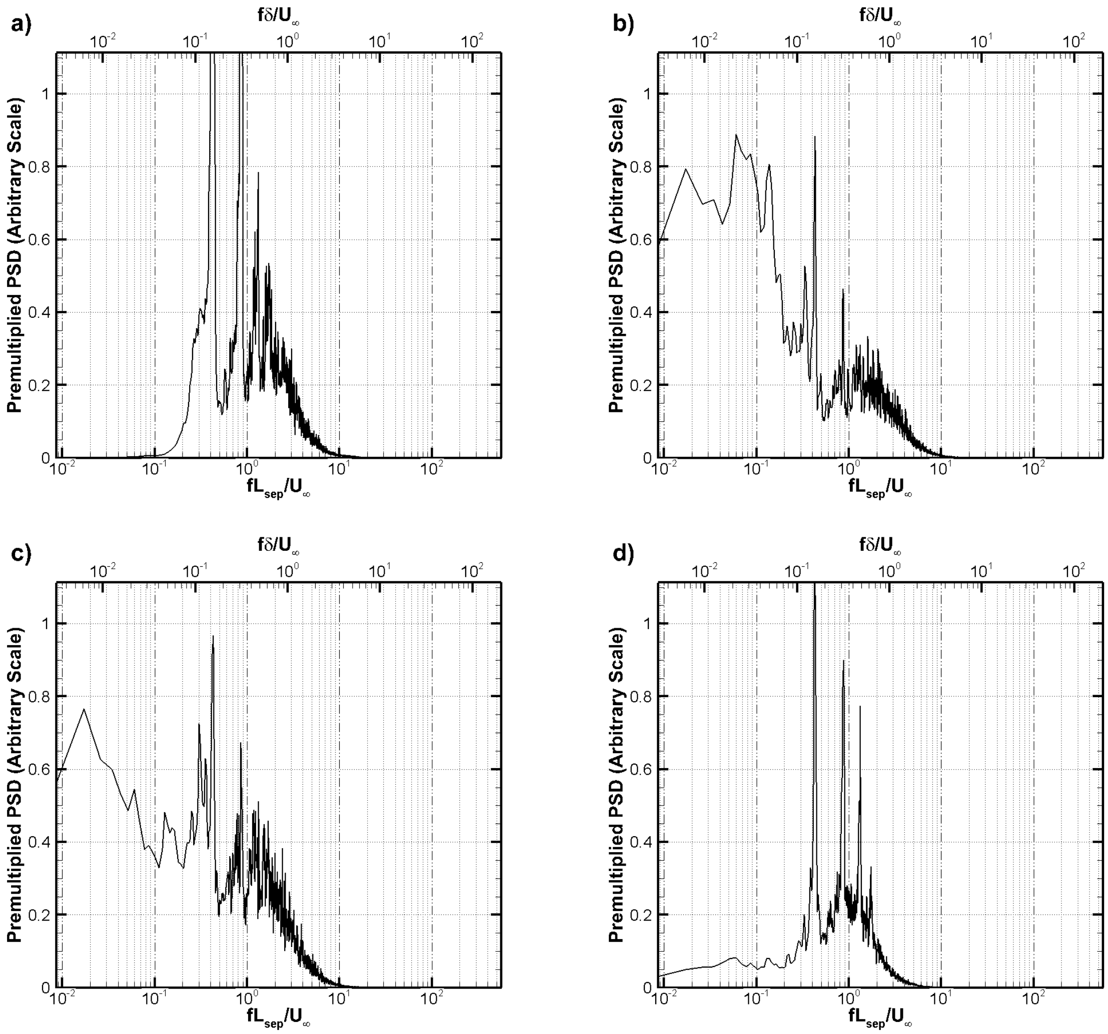

Figure 5. Wall pressure signal spectra taken at: (a) inlet (x^*/δ = -5.05); (b) upstream of average separation (x^*/δ = -2.36); (c) downstream of average separation (x^*/δ = -1.86); and (d) average reattachment (x^*/δ = 0.60).

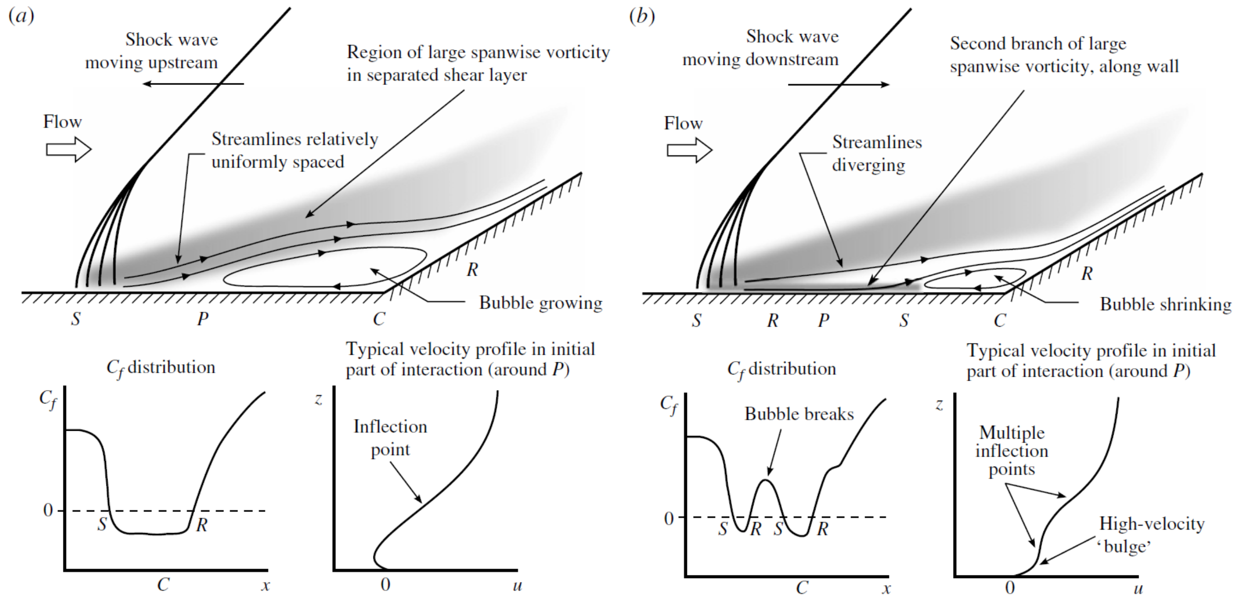

Figure 6. Schematics of the different flow structure observed depending on the phase of the low-frequency motion: (a) bubble growth phase; and (b) bubble collapse phase. (Reproduced from Priebe and Martín, 2012.[12])

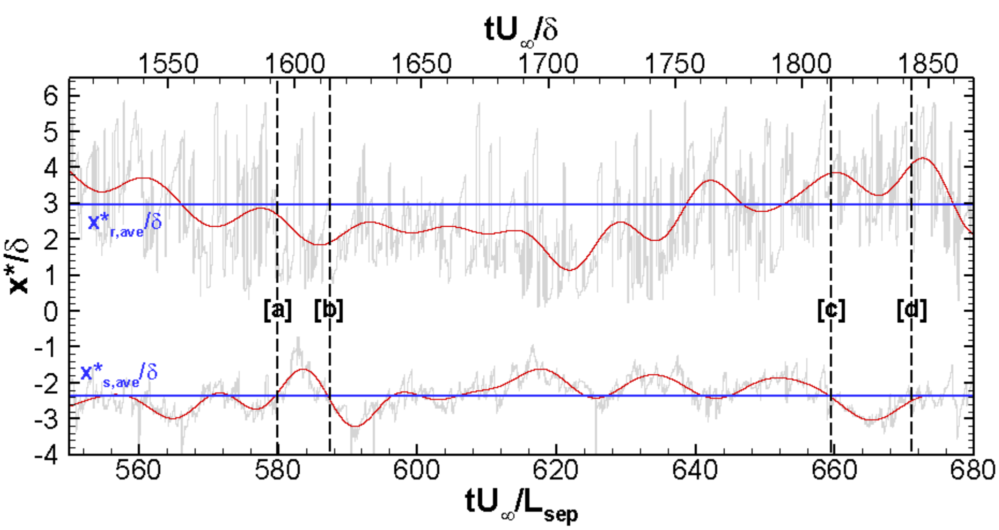

Figure 7. Separation and reattachment location signals for detailed simulation; raw signal in gray (the lowpass filtered signal, cutoff $S_L = 0.22$, in red). Vertical dashed lines indicate instants at which the shock is moving downstream (a, d) and moving upstream (b, c).

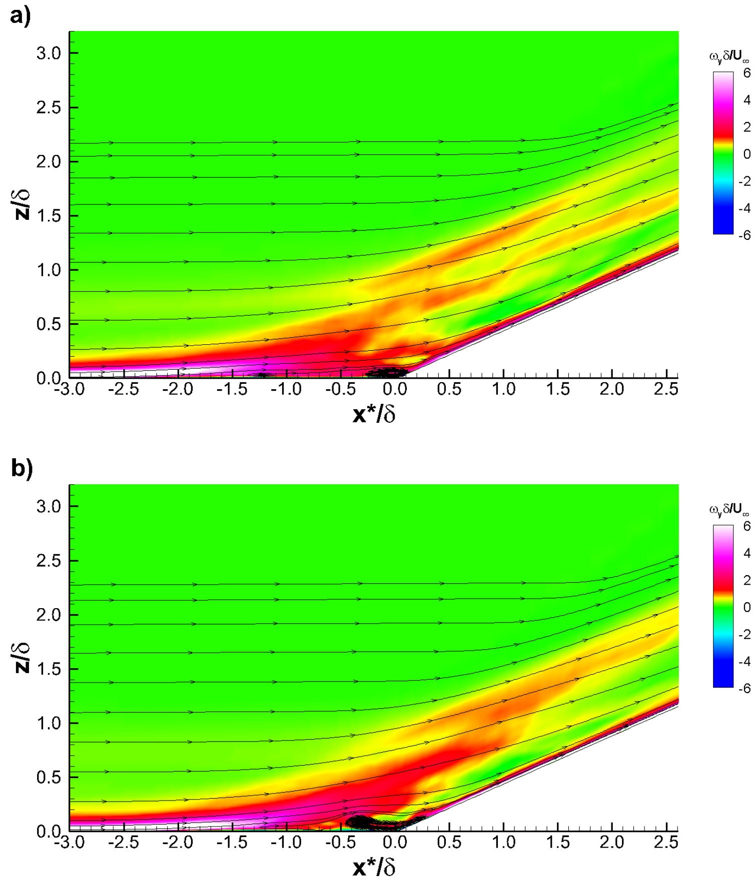

Figure 8. Spanwise-averaged low-pass filtered flow fields at instants indicated previously: (a) downstream shock motion; and (b) upstream shock motion.

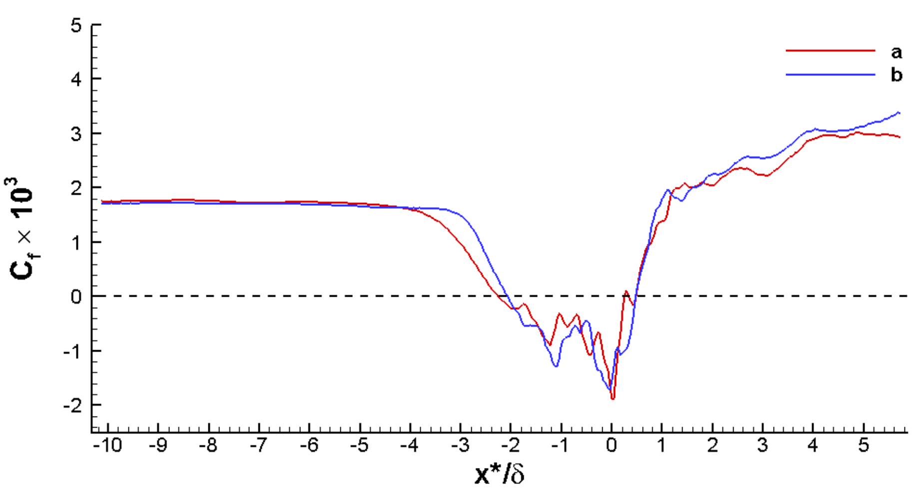

Figure 9. Spanwise-averaged low-pass filtered skin friction coefficient, C_f, at instants indicated previously: downstream shock motion (red), and upstream shock motion (blue)

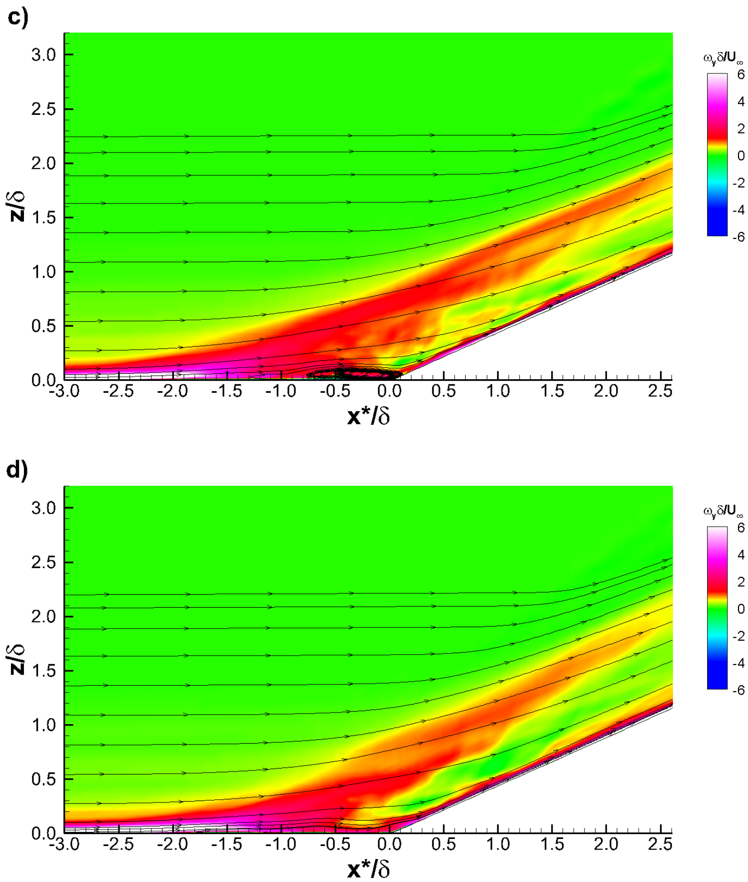

Figure 10. Spanwise-averaged low-pass filtered flow fields at instants indicated previously: (c) upstream shock motion; and (d) downstream shock motion.

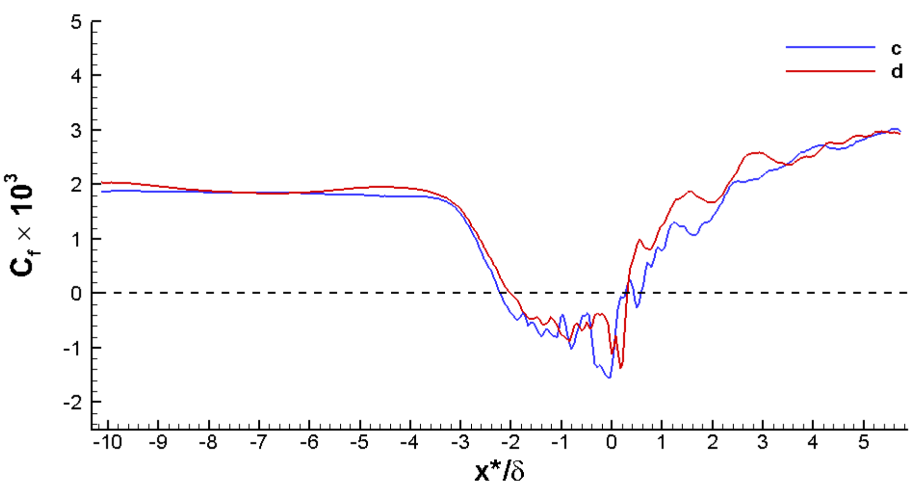

Figure 11. Spanwise-averaged low-pass filtered skin friction coefficient, C_f, at instants indicated previously: downstream shock motion (red), and upstream shock motion (blue)